Analyst

ROYAL SOCIETY OF CHEMISTRY

COMMUNICATION

View Article Online
View Journal | View Issue

Cite this: *Analyst*, 2021, **146**, 1552

Received 27th November 2020,
Accepted 28th December 2020

DOI: 10.1039/d0an02292f

rsc.li/analyst

3D printed smart silk wearable sensors†

Tianshu Chu,‡[a] Huili Wang,‡[b] Yumeng Qiu,[a] Haoxi Luo,[a] Bingfang He,[a] Bin Wu*[c] and Bingbing Gao *[a]

Wearable sensors play a key role in point-of-care testing (POCT) for their flexible and integration capability for sensitive physiological and biochemical sensing. Here, we present a multifunction wearable silk patch with both electronic channels and microchannels by utilizing matrix-assisted sacrificial 3D printing methods. Owing to the unique properties of a composite silk film (polyvinyl alcohol (PVA) and silk fibroin (SF)), the wearable sensors possess excellent tensile properties, self-healing ability and biocompatibility. Multi-layer channel (microfluidics and microcircuit)-integrated silk wearable sensors were then fabricated for simultaneous sensitive sensing of human cancer markers (carcinoembryonic antigen (CEA) and alpha-fetoprotein (AFP)) and motion monitoring. These features of the silk wearable sensors indicate their potential value for sensitive sensing, which will enable them to find broader applications in many fields in POCT, artificial skin and organ-on-a-chip systems.

1. Introduction

Currently, POCT provides an effective means for rapid and simple health monitoring and diagnosis due to its merits of being inexpensive, free of large-scale instruments, disposable and easy to operate. Among various POCT solutions, smart wearable sensors are the most promising and attractive platforms.[1–4] Considerable efforts have been devoted to the fabrication of smart wearable devices. With the integration of microfluidic technology, which has the ability of pumpless delivery and precise liquid control, wearable devices could be endowed with excellent biochemistry detection performance.[5–10] In addition, taking advantage of the rapid development in electronics, microcircuits provide convenience when transforming minor changes into intuitive digital signals. Traditionally, various conductive materials, such as liquid metals, graphene, carbon nanotubes (CNTs) and metal nanowires, have been used in microcircuit fabrication.[11–17] Although great progress has been achieved in smart wearable devices, the fabrication of highly integrated multi-function sensors is still facing great challenges. Moreover, the fabrication methods of microfluidics or microcircuits, such as blade coating, laser engraving and wax printing, only allow channels/circuits to be constructed on a two-dimensional level, which greatly restricts the large-scale integration of wearable sensors. Hence, there is still insurmountable chasm in the production of multifunctional devices integrated with both microfluidics and microcircuits.

In this paper, we propose a novel matrix-assisted sacrificial 3D printing strategy to build complex patterned microchannels with three-dimensional structures based on PVA-SF composite films. 3D printing (additive manufacturing) has gained extensive interest due to its free customization and high precision.[18–22] Patterned microstructures fabricated by 3D printing could thus be able to overcome various limitations of traditional manufacturing through the precise control of a computer and the logic of forming 3D structures. In addition, taking advantage of the excellent biocompatibility and mechanical properties, SF has been widely developed in the fields of medicine and biological materials. The PVA-SF composite film could be endowed with great tensile properties.[23–25] Therefore, the fabrication of a composite film with complex patterned microchannels will bring intriguing developments in smart wearable sensors.

Here, we fabricated a smart flexible silk wearable sensor with multiple functions for human biochemical and motion sensing. Taking advantage of the large amount of dynamic ester bonds between PVA and borax, the composite silk sensors were endowed with self-healing properties.[26–28] The

[a]*School of Pharmaceutical Sciences, Nanjing Tech University, Nanjing 211816, China. E-mail: gaobb@njtech.edu.cn*
[b]*Sir Run Run Hospital, Nanjing Medical University, Nanjing, China*
[c]*College of Biotechnology and Pharmaceutical Engineering, Nanjing Tech University, Nanjing 211816, China. E-mail: wubin1977@njtech.edu.cn*

†Electronic supplementary information (ESI) available. See DOI: 10.1039/d0an02292f

‡These authors contributed equally to this work and should be considered as co-first authors.

patterned microchannel in the hydrogel was constructed by novel matrix-assisted sacrificial 3D printing methods. The multilayer microchannel integrated with PhC microspheres could provide a liquid channel for body fluid transport and sensing, while the microcircuit composed of graphene could serve as a resistance variation-based motion sensor. The results showed that the silk wearable sensor is suitable for simultaneous biochemical sensing (human cancer markers CEA and AFP) and physiology monitoring (motion monitoring). These features demonstrate that silk wearable sensors are highly versatile devices capable of a wide variety of applications.

2. Experimental section

2.1 Materials

Monodisperse SiO_2 nanoparticles with different diameters were self-prepared. A microfluidic droplet system was used to fabricate photonic crystal (PhC) microspheres. Polyvinyl alcohol (PVA), carrageenan, bovine serum albumin (BSA), 2-morpholinoethanesulfonic acid (MES), and *cis*-dichlorodiammine platinum(II) were purchased from Sigma-Aldrich (St Louis, MO). 1-Ethyl-3-(3-dimethylaminepropyl)carbodiimide (EDC), *N*-hydroxysuccinimide (NHS), borax, *N*-hexane and Vaseline were purchased from Chemical Reagent Co., Ltd (Shanghai, China). Graphene electric aqueous slurry (5 wt% graphene) was purchased from Nanjing XFNANO Materials Tech Co. Ltd. Rabbit anti-human CEA, CEA, FITC-labeled mouse anti-human CEA, rabbit anti-human AFP, AFP, and FITC-labeled mouse anti-human AFP were purchased from Santa Cruz Biotechnology (Shanghai) Co.

2.2 Preparation of silk fibroin

Raw silkworm cocoons were shredded, discarded, and poured into boiling Na_2CO_3 solution (0.02 M) for 1 h to obtain degummed fibers. The obtained fibers were then rinsed 3 times with deionized water and dried at 60 °C for 3 h. Silk fibroin was dissolved in LiBr solution (9.3 M) at a ratio of 1 : 4 (w/v) and incubated in a water bath at 65 °C for 1 h, followed by dialysis with deionized water for 3 days. The dialyzed silk fibroin solution was lyophilized, sealed in vacuum, and stored in a refrigerator at −80 °C.

2.3 Fabrication of the PVA–SF precursor

Excess PVA granules were added to deionized water with stirring until they were unable to dissolve at room temperature. The silk fibroin lyophilized powder was made into 4% (w/v) solution in deionized water and then mixed with PVA saturated solution and carrageenan (0.5% w/v) as the precursor fluid.

2.4 3D printing of composite silk films

The precursor was first poured into a Petri dish, and the 3D structures were fabricated with a customized 3D bioprinter (FDM type, nozzle diameter: 0.2–0.4 mm; printing temperature: 30–50 °C; printing speed: 0.5–8 mm s^{-1}; air pump pressure: 0.1 MPa.). The microchannel pattern was designed using 3DSMAX 2020 software. Vaseline was directly extruded into the hydrogel precursor solution, and then the precursor solution was dried into a film under air and immersed in *n*-hexane to remove the Vaseline template, followed by thorough cleaning with ethanol. Finally, the film was immersed in an 8% (w/v) borax solution to obtain a self-healing hydrogel.

2.5 Immunoassay on PhC microspheres

For all kinds of immunoassays on photonic crystal nanospheres, the nanospheres were first treated with MES, EDC, and NHS and then washed with deionized water. Next, antibodies were immobilized on nanospheres by drop-casting and dried in an open area. Then, BSA was added to block excess binding sites and thoroughly washed to remove residues. During detection, the liquid or plasma containing corresponding markers was wicked from the injection hole and allowed to flow along the channels, conjugated with fluorescently labeled antibodies and finally allowed to flow into the sensing areas. After this, fluorescence microscopy was used to capture the fluorescence images of the sensing areas.

2.6 Smart wearable sensors

The silk wearable sensors were attached with PET double-sided tape and then attached on the human wrist for the following test. The electromechanical measurements of the electrical resistance were performed with a multimeter. The participant in the experiments gave his/her full, informed, and voluntary consent to participate in this research. All experiments were performed in compliance with the relevant laws and with the approval of the Scientific Ethical Committee of the School of Pharmaceutical Sciences, Nanjing Tech University.

2.7 Characterization

Scanning electron microscopy (SEM) images were obtained with a field-emission scanning electron microscope (FESEM, Zeiss Ultra Plus). The fluorescence images were captured with a fluorescence microscope (DM2000, Leica). Electromechanical measurements of the electrical resistance were performed with a multimeter (Keithley 2000). The reflection spectra of all PhCs were acquired with a spectrophotometer (Ocean Optics, QE65000).

3. Results and discussion

3.1. Fabrication of patterned composite silk films

Typically, a wearable device with a patterned microchannel inside was fabricated based on the removal of 3D printed sacrificial structure templates. As shown in Fig. 1, to obtain these hollow patterned channels, PVA saturated solution, carrageenan and silk fibroin solution (4% w/v) were first blended to form the hydrogel precursor. After being poured into a rectangular mold, the precursor solution was used as a supporting base for 3D printing. Vaseline was chosen as a sacrificial material for the template material, which could be stably embedded into the silk precursor and could interestingly

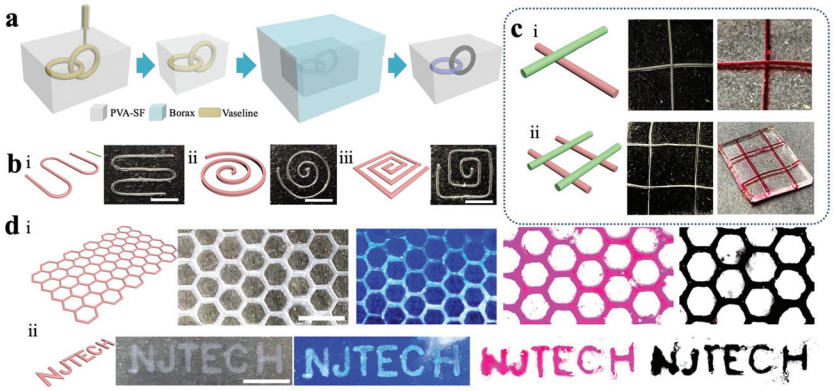

Fig. 1 (a) Schematic illustrations of the fabrication process of a functional composite silk film: Vaseline was directly 3D printed in a PVA–silk fibroin precursor and dried at room temperature, and the Vaseline template was removed, and soaked in borax solution to obtain a composite silk film. (b) Designs (left) and digital images (right) of single-layer (i: U-shaped; ii: spiral; and iii: square spiral) and (c) multilayer (i and ii) patterned microchannels. (d) Designs, photographs, and fluorescence photographs of continuously extruded single-layer patterns and filled with the dye (red) and graphene (black) after being made into microfluidic channels. Scale bar: 0.5 cm.

maintain the printing structure during the drying process; a fused deposition modeling (FDM)-type printer was chosen for the fabrication of microchannel patterns by directly printing the sacrificial material into the base. Then, the silk precursor solution, along with the printed patterns, was dried under air to form a thin film. After removing the sacrificial template using *n*-hexane and alcohol, the obtained film exhibited a patterned microchannel structure inside. The film was further immersed in the borax solution to impart stretching and self-healing abilities.

Vaseline was chosen as the printing ink due to its low solid–liquid conversion temperature, self-supporting ability and hydrophobicity. Vaseline ink could be directly printed as a complex pattern at room temperature and it is immiscible with the hydrophilic hydrogel precursor matrix. More importantly, it can be easily removed using *n*-hexane as a sacrificial material. To improve the printing performance of Vaseline in the silk precursor, we investigated the influence of the precursor liquid (PVA : SF) ratio and the printing speed on the molding effect. As shown in Fig. 2, straight lines were printed, and during the printing process, when the moving speed of the extrusion head is too slow (<0.5 mm s^{-1}), it will cause Vaseline to accumulate in the original place, failing to process. When the moving speed is high (>6 mm s^{-1}), the extruded Vaseline will not have time to adhere to the substrate, resulting in discontinuous lines. Meanwhile, due to the weak bonds between the PVA chains in the precursor, the precursor with a high concentration of PVA has high viscosity; the extrusion head receives a greater shear force and destroys the previously completed printing patterns. With a gradual increase in the proportion of the SF solution, this effect is alleviated, but the supporting ability of the precursor liquid to Vaseline also decreases. The effect of printing speed on the line diameter was also investigated. The results show that under a certain extrusion pressure, the line diameter decreased with the printing speed increase; we chose a printing speed of 2 mm s^{-1} and a precursor solution proportion of 2 : 1 (PVA : SF) for the following experiment.

Owing to the advantages of accurate manufacturing by 3D printing, complex patterns can be printed in the silk film,

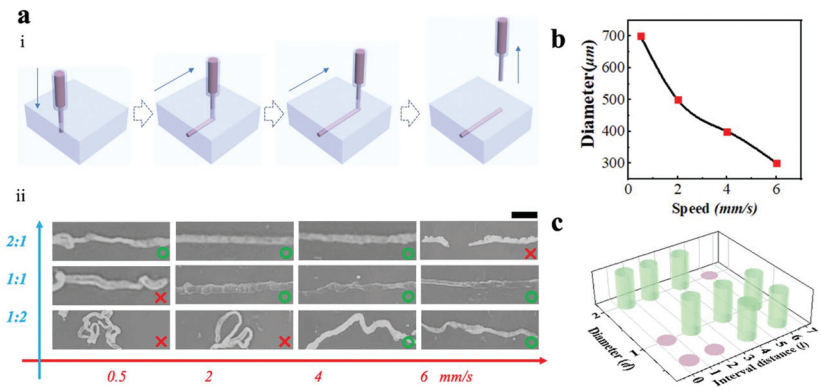

Fig. 2 (a) Schematic diagram of 3D printing (i) and printing performance under different nozzle moving speeds and PVA : SF ratios; scale bar: 0.5 cm (ii); (b) relationship between the printing speed and printing diameter. (c) Diagram of printing performance (i), red: non-printable; green: printable.

which has potential for further utilization as microfluidic channels and microcircuits. As shown in Fig. 1b, Vaseline was patterned as a U-shaped, spiral and square spiral structure by the 3D FDM printing method. Vaseline has a stable structure in the precursor fluid, with a uniform line diameter, no breaks, and no localized ink accumulation even when the moving directions of the nozzle rapidly change at corners. In addition, we further illustrated the printing capabilities of multilayer 3D structures (Fig. 1c). Owing to the self-supporting ability of Vaseline at room temperature, the multilayer lines self-supported without collapsing. A complex cross-linked network could thus be constructed by stacking a single-layer structure. This provides benefits for the integration of wearable devices on a three-dimensional scale.

The construction of microchannels/microcircuits is the core of wearable device manufacturing. The utilization of sacrificial materials to construct complex structures followed by selective removal of materials to obtain inverted structures has been widely used in the manufacture of microstructures. Hollow microchannels in the silk film were later obtained by selectively dissolving the 3D printed Vaseline ink. After the 3D patterning process, the precursor fluid was dried under air and gradually the solvent was lost and a transparent flexible thin film was formed, while the Vaseline patterns remained intact. Then, the dried film was immersed in *n*-hexane, followed by heating to 50 °C to promote the dissolution and removal of the Vaseline template, forming hollow microfluidic channels. As a demonstration, a patterned grid structure and "NJTECH" text channels were constructed and perfused with red and black dyes for the visualization of the channel structure in the film. The result shows that the microfluidic channel made of Vaseline as the sacrificial material still maintains the basic structure and shape details during the drying process. In fact, along with the evaporation of the solvent, a dense cross-linked PVA–SF network gradually formed, which endowed the resulting film with ductility and elasticity. In addition, a barrier layer is formed around the Vaseline line; thus, the integrity of the three-dimensional channel structure could be retained after the ink is removed.

3.2. Self-healing property of composite silk films

The obtained silk film with hollow microchannels was further immersed in a borax solution for full crosslinking. As shown in Fig. 3b, the silk film exhibited transparency and stretching ability. In recent years, there has been a lot of work to produce flexible devices with excellent ductility. Chen *et al.* fabricated a high-stretch-rate (>400%) film by the addition of $CaCl_2$;[29] and Ling *et al.* synthesized novel silk-based strain gauges, which could be stretched up to 1300% without failure.[30] In the work of Yang *et al.*, silk fibroin was added to increase the water uptake of the gel and a stretch rate of over 5000% was achieved.[31] In this work, the changes in tensile properties, structural stability and biocompatibility brought about by the addition of silk fibroin are in good agreement with previous reports. The tensile mechanics test method was utilized to evaluate the mechanical properties of the silk film with

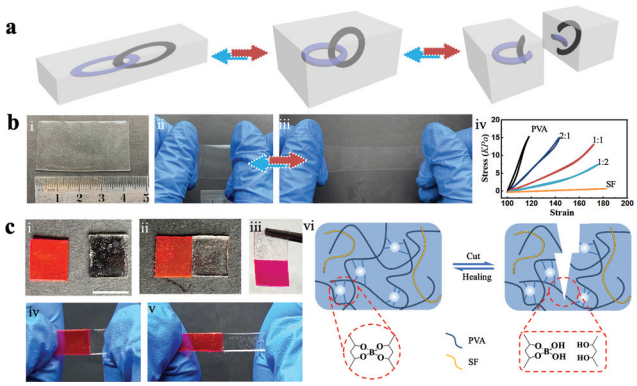

Fig. 3 (a) Schematic diagram of the stretching and self-healing properties of a composite silk film. (b) Image of the hydrogel with high transparency (normal state (i), reversible stretch and recovery state (ii and iii)), and correspondence between the stretching ratio and stress (iv). (c) Image of the hydrogel with (left) and without (right) the red dye (i). Two pieces of the hydrogel are brought into contact and pressed tightly and self-healed (ii and iii), reversible stretch and recovery of the healed film (iv and v), and schematic image of the self-healing mechanism of composite silk film.

different PVA : SF ratios. With the PVA : SF ratios increasing, the stretching ability was significantly improved. To investigate the self-healing ability of the silk film after full crosslinking with borax, two pieces of silk films were prepared, with one doped with a red dye. The boundaries of each film were attached together and were fixed with a clamp for 12 h at room temperature while continuously adding borax to the joint to keep it wet. The two separated films tightly adhered to each other and formed as one film (Fig. 3c). A comparison of the mechanical properties before and after repair is shown in Fig. S1a†. The quantitative relationship between the resistance and device deformation, as well as the cyclic performance, is shown in Fig. S1b and c.† The healed hydrogel maintained its excellent stretching ability and durability. In fact, as a potential property of novel hydrogel devices, the self-healing ability could be realized by metal-ligand coordination, hydrophobic association, π–π stacking or hydrogen-bonding interactions. The self-healing ability was conferred by plenty of hydrogen groups and the dynamic ester bonds formed by the borax–PVA cross-linked network, as illustrated in Fig. 3c-vi.

3.3. Biochemical sensing on a silk wearable sensor

Recently, as a simple, flexible, fast and miniaturized analysis platform, wearable sensors have been used in various physiological and biochemical tests. We further evaluated the capacity of the composite silk film for wearable sensing. As shown in Fig. 4, a double-layer "8-branched" microchannel was fabricated for both biochemical sensing and physiological monitoring. The wearable sensor could be attached on the human wrist for biosensing. As shown in the schematic diagram of the wearable sensor, the sampling point was at the center of the "8-branched" shaped channels, four branches were utilized for biochemical sensing as sensing 1 and sensing

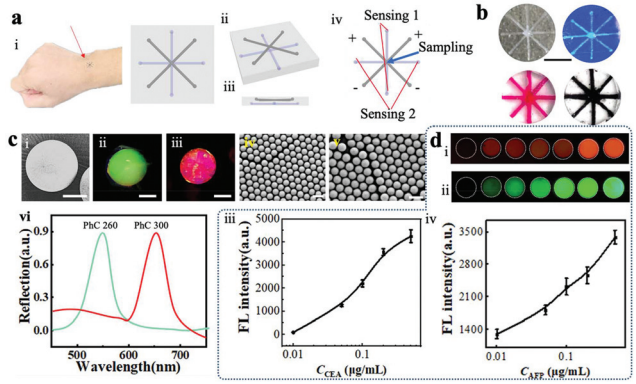

Fig. 4 (a) Smart wearable sensors with multi-layer microchannels for simultaneous physiological and motion detection, optical images of the wearable sensor on the wrist (i), schematic diagram of the wearable sensor (ii, iii and iv). (b) Optical and fluorescence photographs of films with multiple branches and filled with the dye (red) and graphene (black). (c) Optical (ii and iii) and SEM (i, iv and v) images of PhC microspheres (i, iv and v), scale bar: 100 μm for (i–iii) and 500 nm for (iv and v). The reflection peaks of PhC barcodes of PhC260 and PhC300 (vi). (d) Cancer markers detected using the PhC barcodes, fluorescence intensity as a function of CEA (iii) and AFP (iv) concentration and corresponding fluorescence intensity (i and ii). Scale bar: 100 μm.

2, and the other four branches were utilized as microcircuits for the resistance variation-based motion sensor. We first investigated the self-healing performance of the silk-film device with microchannels inside (Fig. S2a†); the result of the liquid fluid performance and resistance response ability in the channel before and after self-healing showed that the liquid flow speed in microchannels and resistance response ability remain unchanged; this proved that the chip has a strong self-healing ability and the functions of its internal components are not affected before and after the repair.

To verify the applicability of wearable devices in POCT, PhC microspheres were used as a sensing unit for immunofluorescence sensing. The PhCs were prepared by microfluidics technology as reported by Zhao.[32] Taking advantage of the orderly arrangement of monodisperse silica nanoparticles, the PhC barcode was endowed with unique PBG (photonic band gap) characteristics and the corresponding reflection spectrum, thus obtaining excellent structural color characteristics. In recent years, detection methods integrated on wearable devices are usually chemical methods. Xiao *et al.* used the pre-embedded glucose oxidase (GOD)–peroxidase–*o*-dianisidine reagents for sensing glucose in sweat with a limit of detection of 0.03 mM.[33] Promphet *et al.* fabricated a sensing system relying on the color change caused by the enzymatic reaction and reached a detection limit of 0.1 mM for glucose.[34] There are also reports of using electrode sensors based on glucose oxidase for detection.[35] Compared with traditional chemical methods, the PhC-based optical detection method has higher sensitivity and lower detection limits, and no complicated external equipment is required. PhC microspheres were placed at the channel end of the wearable sensors (sensing 1 and sensing 2). During detection, the PhC microspheres present different fluorescence signals from the addition of the antigen and fluorescently labeled antibody to PhC barcodes with probes *via* sandwich hybridization, and the fluorescence intensity increased along with the ascension of the target antigen. We then used PhC microspheres as a sensor for the fluorescence detection of two cancer markers (CEA and AFP). A smartphone-based device as our group previously reported[36,37] could be used to carry out the sensing readouts; it can be seen from the image of the fluorescence signal intensity as a function of CEA and AFP concentrations that the concentration of CEA and AFP has a linear relationship with the fluorescence intensity in the range of 10–1000 ng ml^{-1} (Fig. 4d). In this experiment, we use a needle to pierce the skin to obtain blood and its spontaneous flow into the detection area for testing as a proof of concept. However, in future work, microneedles can be combined with our chips to reduce the pain of puncturing the skin. In addition, making our chip semi implantable will greatly expand its application range.

3.4. Motion monitoring on silk wearable sensors

Ideal wearable devices need to integrate excellent electrical performance on a flexible substrate. In the past, many

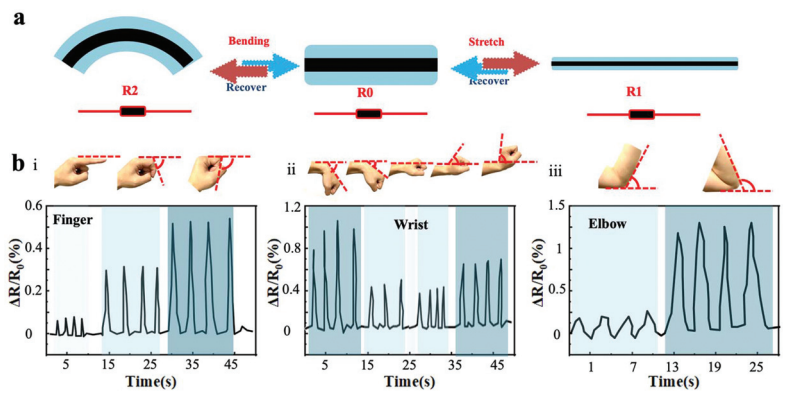

Fig. 5 (a) Schematic diagram of the deformation of the microcircuit sensor during bending and stretching. (b) The relative resistance changes when knuckles (i), wrists (ii) and elbows (iii) are bent at different angles.

researchers have devoted themselves to making flexible conductive films,[38] and there are also reports of filling ionic liquids in microchannels to make elastic conductive fibers.[39] Considering its stretching ability, the composite silk film has potential in building flexible electronic sensors by filling with a graphene-doped hydrogel in the channel. When subjected to bending or stretching, the resistance of the graphene channel showed the corresponding variation; thus, the deformation of the hydrogel device could be reflected by monitoring the resistance change (Fig. 5a). It is noteworthy that, the sensitivity and the relationship between the electrical properties and deformation of this fibrous graphene are in good agreement with the reports on flexible conductive films. In a typical experiment, the 8-branched wearable sensors were infused with graphene on four channels and directly attached to the volunteer's fingers, wrists, and elbows and connected with multimeters. By recording the changes in the resistance in real time, the movement status of each part was reflected (Fig. 5b). Specifically, as the bending angles gradually increase, the resistance increases in real time. Additionally, the hydrogel device also exhibited rapid and stable changes associated with the movement of the finger, wrist and elbow bending during the cycling experiment. These results indicated that the wearable device showed a sensitive and stable electrical sensing ability for dynamic monitoring, which has great potential in real-time human health detection.

4. Conclusion

In summary, we fabricated a multifunction wearable silk patch with both electronic channels and microchannels by utilizing matrix-assisted sacrificial 3D printing methods. The wearable sensors possess excellent tensile properties, self-healing ability and biocompatibility. The multilayer microchannel (microfluidics and microcircuits) integrated with PhC microspheres could provide a liquid channel for body fluid transport and sensing, while the microcircuit composed of graphene could serve as a resistance variation-based motion sensor. The results showed that the silk wearable sensor is suitable for simultaneous biochemical sensing (human cancer markers CEA and AFP) and physiology monitoring (motion monitoring). The developed silk sensors are promising in a variety of applications, such as personal care, POCT and environmental monitoring.

Conflicts of interest

The authors declare that they have no conflict of interest.

Acknowledgements

We gratefully acknowledge the financial support from the National Key R&D Program of China (2019YFA09005200), the National Natural Science Foundation of China (81673321 and 21776135), the Natural Science Foundation of Jiangsu Province (BK20200703), the Natural Science Research of Jiangsu Higher Education Institutions of China (20KJB416011) and the special funds for the introduction of talents of Nanjing Tech University (39828122).

References

1 A. K. Yetisen, J. L. Martinez-Hurtado, B. Ünal, A. Khademhosseini and H. Butt, *Adv. Mater.*, 2018, **30**, 1706910.
2 A. Miyamoto, S. Lee, N. F. Cooray, S. Lee, M. Mori, N. Matsuhisa, H. Jin, L. Yoda, T. Yokota, A. Itoh, M. Sekino, H. Kawasaki, T. Ebihara, M. Amagai and T. Someya, *Nat. Nanotechnol.*, 2017, **12**, 907–913.
3 G. A. Salvatore, J. Sülzle, F. Dalla Valle, G. Cantarella, F. Robotti, P. Jokic, S. Knobelspies, A. Daus, L. Büthe, L. Petti, N. Kirchgessner, R. Hopf, M. Magno and G. Tröster, *Adv. Funct. Mater.*, 2017, **27**, 1702390.
4 C. Pang, J. H. Koo, A. Nguyen, J. M. Caves, M.-G. Kim, A. Chortos, K. Kim, P. J. Wang, J. B.-H. Tok and Z. Bao, *Adv. Mater.*, 2015, **27**, 634–640.
5 B. Hu, J. Li, L. Mou, Y. Liu, J. Deng, W. Qian, J. Sun, R. Cha and X. Jiang, *Lab Chip*, 2017, **17**, 2225–2234.
6 T. Laksanasopin, T. W. Guo, S. Nayak, A. A. Sridhara, S. Xie, O. O. Olowookere, P. Cadinu, F. Meng, N. H. Chee, J. Kim, C. D. Chin, E. Munyazesa, P. Mugwaneza, A. J. Rai, V. Mugisha, A. R. Castro, D. Steinmiller, V. Linder, J. E. Justman, S. Nsanzimana and S. K. Sia, *Sci. Transl. Med.*, 2015, **7**, 273re271.
7 J. Choi, D. Kang, S. Han, S. B. Kim and J. A. Rogers, *Adv. Healthcare Mater.*, 2017, **6**, 1601355.
8 Y. Sekine, S. B. Kim, Y. Zhang, A. J. Bandodkar, S. Xu, J. Choi, M. Irie, T. R. Ray, P. Kohli, N. Kozai, T. Sugita, Y. Wu, K. Lee, K.-T. Lee, R. Ghaffari and J. A. Rogers, *Lab Chip*, 2018, **18**, 2178–2186.
9 L. Sun, F. Bian, Y. Wang, Y. Wang, X. Zhang and Y. Zhao, *Proc. Natl. Acad. Sci. U. S. A.*, 2020, **117**, 4527–4532.
10 X. Zhang, G. Chen, Y. Liu, L. Sun, L. Sun and Y. Zhao, *ACS Nano*, 2020, **14**, 5901–5908.
11 S.-Z. Guo, K. Qiu, F. Meng, S. H. Park and M. C. McAlpine, *Adv. Mater.*, 2017, **29**, 1701218.
12 H. Ota, S. Emaminejad, Y. Gao, A. Zhao, E. Wu, S. Challa, K. Chen, H. M. Fahad, A. K. Jha, D. Kiriya, W. Gao, H. Shiraki, K. Morioka, A. R. Ferguson, K. E. Healy, R. W. Davis and A. Javey, *Adv. Mater. Technol.*, 2016, **1**, 1600013.
13 J. Kim, M. Kim, M.-S. Lee, K. Kim, S. Ji, Y.-T. Kim, J. Park, K. Na, K.-H. Bae, H. Kim, F. Bien, C. Young Lee and J.-U. Park, *Nat. Commun.*, 2017, **8**, 14997.
14 T. Q. Trung, S. Ramasundaram, B.-U. Hwang and N.-E. Lee, *Adv. Mater.*, 2016, **28**, 502–509.
15 Y. Yu, J. Guo, B. Ma, D. Zhang and Y. Zhao, *Sci. Bull.*, 2020, **65**, 1752–1759.
16 Y. Wang, Y. Yu, J. Guo, Z. Zhang, X. Zhang and Y. Zhao, *Adv. Funct. Mater.*, 2020, **30**, 2000151.

17 Z. Zhang, Z. Chen, Y. Wang and Y. Zhao, *Proc. Natl. Acad. Sci. U. S. A.*, 2020, **117**, 18310–18316.
18 H. Gong, B. P. Bickham, A. T. Woolley and G. P. Nordin, *Lab Chip*, 2017, **17**, 2899–2909.
19 I. C. Samper, S. A. N. Gowers, M. L. Rogers, D.-S. R. K. Murray, S. L. Jewell, C. Pahl, A. J. Strong and M. G. Boutelle, *Lab Chip*, 2019, **19**, 2038–2048.
20 J. T. Muth, D. M. Vogt, R. L. Truby, Y. Mengüç, D. B. Kolesky, R. J. Wood and J. A. Lewis, *Adv. Mater.*, 2014, **26**, 6307–6312.
21 J. Qiu, Q. Gao, H. Zhao, J. Fu and Y. He, *ACS Biomater. Sci. Eng.*, 2017, **3**, 2606–2616.
22 D. Lei, Y. Yang, Z. Liu, B. Yang, W. Gong, S. Chen, S. Wang, L. Sun, B. Song, H. Xuan, X. Mo, B. Sun, S. Li, Q. Yang, S. Huang, S. Chen, Y. Ma, W. Liu, C. He, B. Zhu, E. M. Jeffries, F.-L. Qing, X. Ye, Q. Zhao and Z. You, *Mater. Horiz.*, 2019, **6**, 1197–1206.
23 Q. Wang, S. Ling, X. Liang, H. Wang, H. Lu and Y. Zhang, *Adv. Funct. Mater.*, 2019, **29**, 1808695.
24 L. Shi, F. Wang, W. Zhu, Z. Xu, S. Fuchs, J. Hilborn, L. Zhu, Q. Ma, Y. Wang, X. Weng and D. A. Ossipov, *Adv. Funct. Mater.*, 2017, **27**, 1700591.
25 J. B. Costa, J. Silva-Correia, J. M. Oliveira and R. L. Reis, *Adv. Healthcare Mater.*, 2017, **6**, 1701021.
26 Z. Wang, F. Tao and Q. Pan, *J. Mater. Chem. A*, 2016, **4**, 17732–17739.
27 B. Lu, F. Lin, X. Jiang, J. Cheng, Q. Lu, J. Song, C. Chen and B. Huang, *ACS Sustainable Chem. Eng.*, 2017, **5**, 948–956.
28 W.-P. Chen, D.-Z. Hao, W.-J. Hao, X.-L. Guo and L. Jiang, *ACS Appl. Mater. Interfaces*, 2018, **10**, 1258–1265.
29 G. Chen, N. Matsuhisa, Z. Liu, D. Qi, P. Cai, Y. Jiang, C. Wan, Y. Cui, W. R. Leow, Z. Liu, S. Gong, K.-Q. Zhang, Y. Cheng and X. Chen, *Adv. Mater.*, 2018, **30**, 1800129.
30 S. Ling, Q. Zhang, D. L. Kaplan, F. Omenetto, M. J. Buehler and Z. Qin, *Lab Chip*, 2016, **16**, 2459–2466.
31 N. Yang, P. Qi, J. Ren, H. Yu, S. Liu, J. Li, W. Chen, D. L. Kaplan and S. Ling, *ACS Appl. Mater. Interfaces*, 2019, **11**, 23632–23638.
32 Y. Xu, X. Zhang, C. Luan, H. Wang, B. Chen and Y. Zhao, *Biosens. Bioelectron.*, 2017, **87**, 264–270.
33 J. Xiao, Y. Liu, L. Su, D. Zhao, L. Zhao and X. Zhang, *Anal. Chem.*, 2019, **91**, 14803–14807.
34 N. Promphet, J. P. Hinestroza, P. Rattanawaleedirojn, N. Soatthiyanon, K. Siralertmukul, P. Potiyaraj and N. Rodthongkum, *Sens. Actuators, B*, 2020, **321**, 128549.
35 T. Arakawa, K. Tomoto, H. Nitta, K. Toma, S. Takeuchi, T. Sekita, S. Minakuchi and K. Mitsubayashi, *Anal. Chem.*, 2020, **92**, 12201–12207.
36 Z. He, A. Elbaz, B. Gao, J. Zhang, E. Su and Z. Gu, *Adv. Healthcare Mater.*, 2018, **7**, 1701306.
37 J. Chi, B. Gao, M. Sun, F. Zhang, E. Su, H. Liu and Z. Gu, *Anal. Chem.*, 2017, **89**, 7727–7733.
38 C. Ye, J. Wang, Y. Xu, K. Zheng, X. Wang, S. Ling and D. L. Kaplan, *Adv. Mater. Technol.*, 2019, **4**, 1800141.
39 Y. Wang, S. Gong, S. J. Wang, G. P. Simon and W. Cheng, *Mater. Horiz.*, 2016, **3**, 208–213.